agriculture

MDPI

Article

Failure State Identification and Fault Diagnosis Method of Vibrating Screen Bolt Under Multiple Excitation of Combine Harvester

Jiaojiao Xu [1,*], Tiantian Jing [2], Meng Fang [2], Pengcheng Li [2] and Zhong Tang [2,3]

1 Higher Vocational Technical College, Shanghai University of Engineering Science, Shanghai 200437, China
2 School of Agricultural Engineering, Jiangsu University, Zhenjiang 212013, China; jtt1632023@163.com (T.J.); 18851289385@163.com (M.F.); 2212016046@stmail.ujs.edu.cn (P.L.); zht@ujs.edu.cn (Z.T.)
3 Key Laboratory of Modern Agricultural Equipment and Technology, Ministry of Education, Jiangsu University, Zhenjiang 212013, China
* Correspondence: jiaojiaoxu525@outlook.com

Abstract: The demanding operational conditions of combine harvesters induce substantial vibrations and component degradation, significantly impacting harvesting efficiency, safety, and overall machine reliability. Bolt loosening, a critical failure mode at the joints of various working parts of combine harvesters, is a prevalent concern. The complexity and heterogeneity of vibration signals in these machines present a considerable challenge for the timely and accurate detection of bolt loosening. This paper proposes a novel methodology for identifying and diagnosing vibrating screen bolt failure states under multiple excitation conditions, specifically tailored for the 4LZY-1.8(PRO688Q) combine harvester. The study initially analyzes the critical torque associated with bolt connection failure. Subsequently, vibration signals are acquired from the bolt connection of the vibrating screen, and time-frequency analysis is performed to characterize the degree of bolt loosening, the predominant vibration direction, and the causative frequency components. A high-dimensional feature matrix is then constructed utilizing a Gaussian kernel function. The efficacy of the proposed methodology is evaluated through training and testing a classification decision model. This study provides a robust theoretical foundation for the vibration-based fault diagnosis of bolt structures in combine harvesters.

Keywords: combine harvester; bolt failure state recognition; time-frequency characteristics; support vector machine; multi-fusion matrix

check for updates

Academic Editor: Ju-Seok Nam

Received: 21 December 2024
Revised: 13 February 2025
Accepted: 18 February 2025
Published: 20 February 2025

Citation: Xu, J.; Jing, T.; Fang, M.; Li, P.; Tang, Z. Failure State Identification and Fault Diagnosis Method of Vibrating Screen Bolt Under Multiple Excitation of Combine Harvester. *Agriculture* **2025**, *15*, 455. https://doi.org/10.3390/agriculture15050455

1. Introduction

Combine harvesters, characterized by complex working mechanisms including cutting platforms, conveying troughs, and vibrating screens, are subjected to intricate and severe loads during the harvesting process, impacting the machine's operational efficiency [1,2]. This leads to issues such as significant whole-machine vibration and premature component damage, severely affecting harvesting efficiency and the overall safety and reliability of the machine [3–5]. As combine harvesters evolve towards larger, faster, more efficient, and intelligent designs, it is increasingly crucial to investigate the vibration characteristics and identification methods of their various mechanisms for structural optimization [3–5]. Bolted structures, due to their simplicity, standardization, and ease of replacement, serve as the primary connection method between the working components of combine harvesters. However, intense and continuous multi-source vibrations can lead to fatigue failure in bolted connections [6]. Statistics indicate that approximately 80% of structural failures are attributed to fatigue, making bolt loosening a major failure mode at the connection points of various working parts [7–9]. In recent years, scholars have conducted extensive research on bolt loosening analysis, including mechanical modeling and vibration signal identification.

Currently, most domestic researchers analyze the vibration characteristics of individual mechanisms by disassembling the devices and structures on the entire machine. Simultaneously, scholars have analyzed the mechanical properties and established dynamic models of bolted structures based on the operating conditions of bolted joints [10–12]. Mechanical analysis primarily includes calculations of deformation within the allowable range of material performance indicators under static loads, pre-tightening force parameters, and static response distributions [13–15]. The establishment and solution of dynamic models can be categorized into contact surface micro-tangential response models, lumped mass models for axial macroscopic vibrations, and torsional vibration dynamic models [16–18]. Moreover, by utilizing intuitive finite element models to simulate realistic load environments, the vibration response characteristics of bolted joints in working components can be obtained [19,20].

Influenced by field operating environments, multiple vibration sources, and complex transmissions, the vibration response signals of bolted structures in combine harvesters change significantly after failure. The extracted feature signals require processing to remove interference and noise [21–23]. To prevent noise interference with normal signals, it is necessary to decompose the vibration signals [24,25]. Time-frequency analysis methods are widely used in the analysis of spectral characteristics of impulse and vibration signals [26,27]. Variational mode decomposition (VMD), with its complete mathematical theory and optimal reconstruction characteristics, ensures superior signal decomposition performance [28,29] and has been applied in signal extraction for combine harvesters [30]. Support vector machine (SVM) is a primary method for identifying bolt failure states through the analysis of vibration signals [31–33]. However, before training and testing bolt failure state data, it is necessary to optimize model parameters and data structures to enhance model identification accuracy [34–36]. By using optimization algorithms to find the optimal parameters, the accuracy of bolt structure failure state identification is significantly improved [37–39].

In conclusion, the complex operational environment and dynamic loading conditions inherent in combine harvesters render them susceptible to connection bolt failures. Existing methodologies for bolt loosening identification often demonstrate limitations, particularly concerning the effective integration of optimization algorithms to enhance parameter selection. To address these shortcomings, this paper introduces a novel approach for the identification of failure states and fault diagnosis within the vibrating screen bolt connections under multiple excitation scenarios. Initially, a finite element model of the bolted joint, representative of the combine harvester's structure, is constructed to facilitate the analysis of critical torque thresholds associated with bolt failure. Subsequently, vibration signals acquired at the bolted joint of the vibrating screen undergo comprehensive analysis, enabling the quantification of loosening severity, the identification of the dominant vibration direction, and the characterization of the underlying frequency components. Furthermore, leveraging a Gaussian kernel function, a classification decision model based on the support vector machine (SVM) is developed for the classification and identification of bolt loosening states.

2. Material and Methods

2.1. Combine Harvester Vibrating Screen Bolt Model with Loose Torque

Bolted connections are broadly categorized into two primary types: conventional bolted connections and pin-hole bolted connections. In conventional bolted configurations, the applied tensile force within the bolt, resulting from nut tightening, generates frictional resistance at the joint interfaces, effectively counteracting transverse external forces. Conversely, in pin-hole connections, external forces are directly imposed upon the bolt, and the inherent shear strength of the bolt itself bears the lateral load. The vibrating screen assembly of the combine harvester predominantly employs conventional bolted connections, typically utilizing coarse-threaded bolts, as illustrated in Figures 1 and 2.

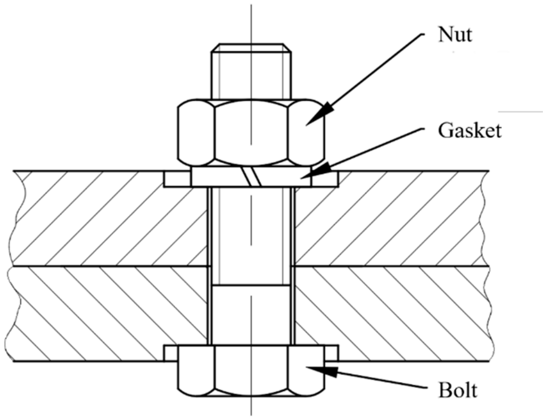

Figure 1. Normal bolt connection.

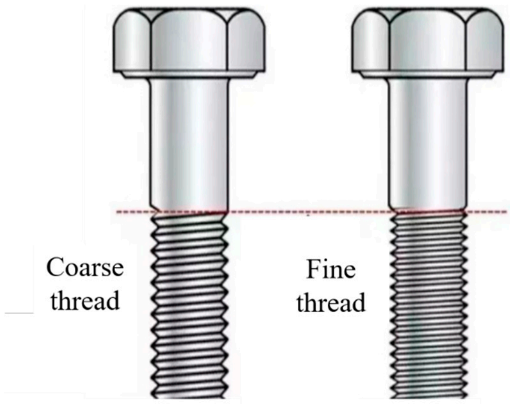

Figure 2. Comparison of coarse and fine tooth bolts.

In bolted connections, the preload causes frictional constraints between the joint structures to keep the structure stable. When the frictional restraint is broken, the bolted connection fails, resulting in loosening. The force analysis of the threaded pair was carried out to simplify the model to an inclined slide model, as shown in Figure 3. The bevel and slider represent the thread of the bolt and nut, and the slope angle of the bevel is equivalent to the thread angle λ of the thread.

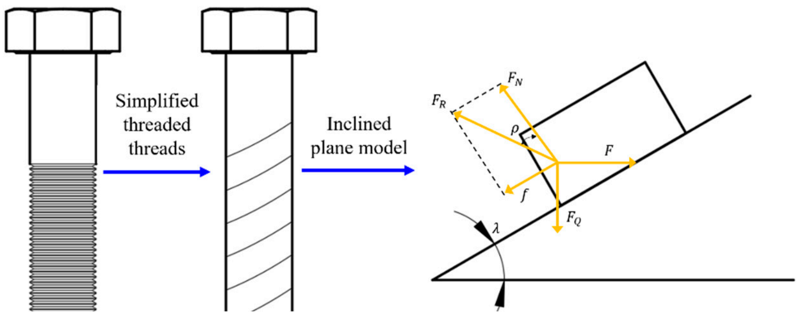

Figure 3. Ramp model of the bolt.

From the Figure 3, it can be seen that the bolt is subjected to the preload force F_Q exerted by the nut on the clamped member, the friction force f down along the inclined plane, the support force F_N provided by the inclined plane, and the horizontal combined force of tightening F. Where the friction force f down along the inclined plane and the support force F_N provided by the inclined plane can be synthesized into the support force F_R provided by the inclined plane, and the angle between F_R and F_N is known as the equivalent friction angle, which satisfies the relationship of Equation (1).

$$\tan\rho = \frac{\mu_1}{\cos\beta} \tag{1}$$

where ρ is the equivalent friction angle between threaded parts; β is the tooth side angle, the ordinary metric thread is usually 30°; μ_1 is the friction coefficient between threaded parts.

According to the equilibrium of force:

$$F = F_Q \tan(\lambda + \rho) \tag{2}$$

$$\lambda = \frac{P}{\pi d_2} \tag{3}$$

where λ is the thread rise angle; P is the pitch; d_2 is the thread center diameter.

The individual diameters of the threaded pair are shown in Figure 4, and the contact surface face force is as follows:

$$f_{s1} = \frac{F}{\pi\left(\frac{d}{2}\right)^2 + \pi\left(\frac{d_1}{2}\right)^2} \tag{4}$$

where d is the nominal diameter of the thread; d_1 is the small diameter of the bolt.

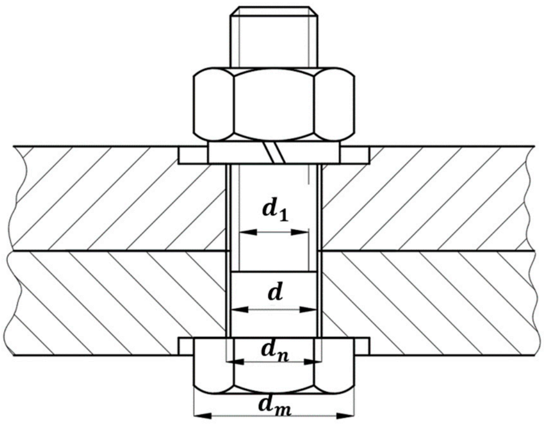

Figure 4. Individual diameters of threaded parts.

Integrating along the inner ring radial to the outer diameter of the ring, the friction moment between the threaded pair is obtained as follows:

$$T_1 = \int_{\frac{d_1}{2}}^{\frac{d}{2}} (f_{s1} \times 2\pi r \mathrm{d}r) \times r = \frac{1}{3} F_Q \tan(\lambda + \rho) \frac{(d^3 - {d_1}^3)}{(d^2 - {d_1}^2)} \tag{5}$$

where r is the radius of the distance from the microcircle to the center of the circle.

The support force between the bolt and the connected member is as follows:

$$f_{s2} = \frac{F_Q}{\pi\left(\frac{d_m}{2}\right)^2 + \pi\left(\frac{d_n}{2}\right)^2} \tag{6}$$

where d_m is the diameter of the contact surface bolt; d_n is the diameter of the contact surface hole.

The friction moment between the bolt and the connected part is as follows:

$$T_2 = \int_{\frac{d_n}{2}}^{\frac{d_m}{2}} \mu_2(f_{s2} \times 2\pi r \mathrm{d}r) \times r = \frac{1}{3}\mu_2 F_Q \tan(\lambda+\rho)\frac{({d_m}^3 - {d_n}^3)}{({d_m}^2 - {d_n}^2)} \tag{7}$$

where r is the radius of the distance from the microcircle to the center of the circle; μ_2 is the friction coefficient of the contact surface.

In summary, the bolt-loosening torque is as follows:

$$T_s = T_1 + T_2 = \frac{1}{3}F_Q\tan(\lambda+\rho)\frac{\left(d^3 - {d_1}^3\right)}{\left(d^2 - {d_1}^2\right)} + \frac{1}{3}\mu_2 F_Q\tan(\lambda+\rho)\frac{({d_m}^3 - {d_n}^3)}{({d_m}^2 - {d_n}^2)} \tag{8}$$

2.2. Bolt Failure State Identification Method

When the bolt is loosened, the vibration signal will also change due to the change of force and load. Therefore, in this paper, the collected vibration signal is used as the input, and a signal recognition method for the failure state of bolts is established through mechanical analysis of the critical failure state.

2.2.1. Feature Extraction Based on Optimized VMD Energy Entropy

The variational mode decomposition (VMD) paradigm decomposes a complex signal into a summation of spectrally localized modal constituents, denoted $\nu_k(t)$, each possessing a characteristic center frequency, ω_k. Employing the Hilbert transform on each modal element yields its unilateral frequency profile. By means of a mixing process coupled with an estimation of the central frequency, the single-sided spectrum of each component undergoes modulation to the baseband. Subsequently, Gaussian smoothing is applied to the L2 regularized gradient of the demodulated signal, thereby enabling the extraction of the power component's bandwidth. The corresponding variational formulation, subject to specific constraints, is articulated as follows:

$$\begin{cases} \min\limits_{\{\nu_k\},\{\omega_k\}} \left\{ \sum_k \left\| \partial_t \left[\left(\delta(t) + \frac{j}{\pi t} \right) \nu_k(t) \right] \mathrm{e}^{-j^{\omega}kt} \right\|^2 \right\} \\ \qquad s.t.\ \sum_k \nu_k = f \end{cases} \tag{9}$$

where $\{\nu_k\}$ is the decomposed IMF component and $\{\omega_k\}$ is the center frequency of the IMF component.

The Lagrangian penalty operator λ and the penalty parameter α are introduced to transform the constrained variational problem into an unconstrained variational problem, as shown in Equation (10).

$$L(\{\nu_k\},\ \{\omega_k\},\ \lambda) = \alpha\sum_k \left\| \partial_t \left[(\delta(t) + \frac{j}{\pi t})\nu_k(t) \right] e^{-j^{\omega}kt} \right\|^2 + \|f(t) - \sum_k \nu_k(t)\|_2^2 + \langle \lambda(t),\ f(t) - \sum_k \nu_k(t) \rangle \tag{10}$$

The alternating direction method of multipliers (ADMM) is used to find the saddle point of Equation (10). The steps are as follows:

(1) Initialize the parameters ν_1, ω_1, λ_1, and n. The initial value of n is set to 0;

(2) Set up the cyclic process so that $n = n + 1$ and ν_k^{n+1}, ω_k^{n+1}, and $\lambda(t)$ are updated according to Equations (11)–(13).

$$\hat{\nu}_k^{n+1}(\omega) = \frac{\hat{f}(\omega) - \sum_{i \neq k} \hat{\nu}_i + \hat{\tau}(\omega)/2}{1 + 2\alpha(\omega - \omega_k)^2} \tag{11}$$

$$\omega_k^{n+1} = \frac{\int_0^\infty \omega |\hat{v}_i(\omega)|^2 d\omega}{\int_0^\infty |\hat{v}_i(\omega)|^2 d\omega} \tag{12}$$

$$\hat{\lambda}^{n+1}(\omega) \leftarrow \hat{\lambda}^n(\omega) + \tau((\hat{f}(\omega) - \sum_k \hat{v}_k^{n+1}(\omega)) \tag{13}$$

(3) When the components satisfy Equation (14), the solution is complete.

$$\sum_k \frac{\|\hat{v}_k^{n+1}(\omega) - \hat{v}_k^n(\omega)\|_2^2}{\|\hat{v}_k^n(\omega)\|_2^2} < \varepsilon \tag{14}$$

2.2.2. VMD Parameter Optimization Based on WOA Envelope Entropy

The efficacy of the VMD decomposition is primarily contingent upon the user-defined number of modes. Insufficient mode selection can lead to the omission of critical information present in the original signal, thereby compromising the fidelity of subsequent predictive analyses. Conversely, an excessively large mode number can engender frequency proximity between adjacent modal components, resulting in modal redundancy or the introduction of extraneous noise [40–43]. Recognizing the inherent spectral diversity among the modes, we employ an optimization strategy, synergizing an algorithmic framework with entropy-based criteria, to refine the VMD parameters. This approach seeks to identify the optimal parameter configuration, thereby facilitating accurate information feature extraction.

The whale optimization algorithm (WOA), a relatively recent development in the realm of swarm intelligence optimization, was formulated to emulate the foraging tactics of humpback whales within their marine habitat [44,45]. The core operational principles of this algorithm are elucidated as follows:

(1) Rounding up prey

$$D = |C \cdot X^*(t) - X(t)| \tag{15}$$

$$X(t+1) = X^*(t) - AD \tag{16}$$

$$A = 2ar_1 - a \tag{17}$$

$$C = 2r_2 \tag{18}$$

$$a = 2 - \frac{2t}{t_{max}} \tag{19}$$

where t is the number of iterations; A and C are the denotation coefficients; $X^*(t)$ denotes the best whale position so far; $X(t)$ denotes the current whale position; r_1 and r_2 are random numbers in (0, 1), and the value of a decreases linearly from 2–0, and t_{max} is the maximum number of iterations.

(2) Bubble netting

$$X(t+1) = D_p e^{bl} \cos(2\pi l) + X^*(t) \tag{20}$$

$$D_p = |X^*(t) - X(t)| \tag{21}$$

where D_p is the distance between the whale and the prey; b is a constant that defines the shape of the spiral; and l is a random number in $(-1, 1)$.

(3) Searching for prey

$$D = |CX_{rand}(t) - X(t)| \tag{22}$$

$$X(t+1) = X_{rand}(t) - AD \tag{23}$$

where $X_{rand}(t)$ is the randomly selected whale position vector. The algorithm is set to randomly select a search agent when $A \geq 1$, and update the position of other whales based on the randomly selected whale position, forcing the whale to deviate from the prey, by which to find more suitable prey, which can strengthen the exploration ability of the algorithm to enable the WOA algorithm to perform a global search, The specific process is shown in Figure 5.

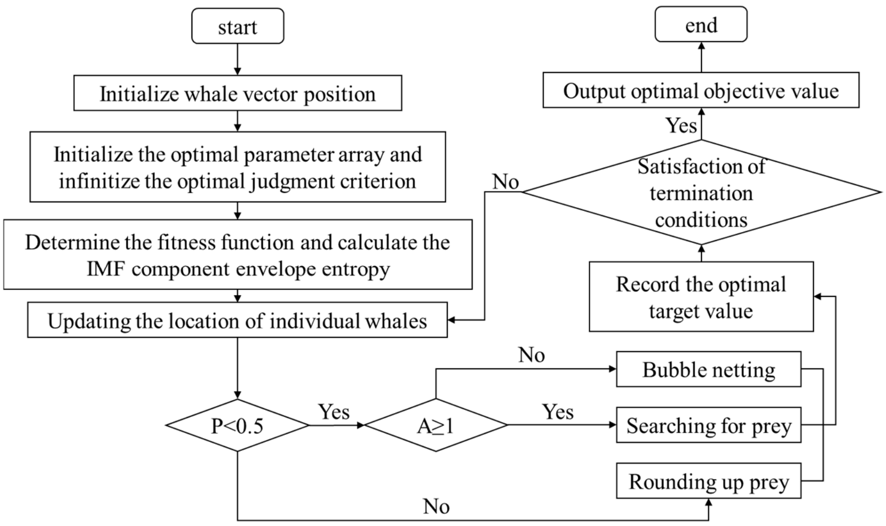

Figure 5. Flowchart of WOA algorithm.

2.2.3. Bolt Loosening State Recognition Based on Support Vector Machine

Support vector machine (SVM) is a binary classification model, which can be defined as a linear classifier with the largest interval in the feature space, and transforms the problem into a convex quadratic programming problem [46,47]. SVM was originally used to solve linear classification problems, but since the kernel method was added in the 1990s, it can also effectively solve nonlinear problems and can adapt to data sets with small sample sizes and high feature dimensions.

SVM finds the optimal hyperplane $\omega^T x + b = 0$ and the corresponding classification decision function $f(x) = sign(\omega^T x + b)$ through dataset training. The SVM classification principle of linear separable and linear non-separable data can be represented by Figure 6. The large probability of the characteristic matrix of the bolt failure state of the vibrating screen belongs to the linear inseparable category. Therefore, it is necessary to introduce a kernel function to perform high-dimensional mapping of the data so that the data can obtain a discriminative optimal hyperplane in the high-dimensional space so as to complete the identification of the bolt failure state.

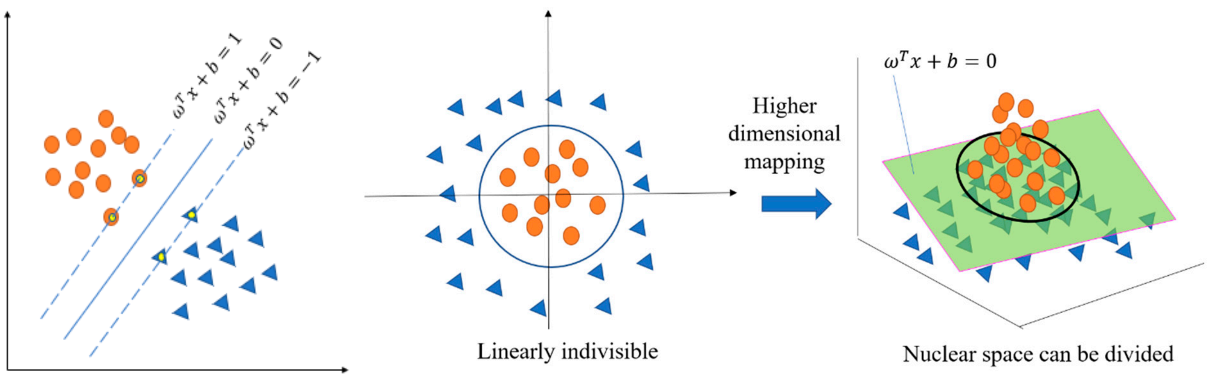

(**a**) Data linearly separable case (**b**) Data linearly indivisible case

Figure 6. Illustration of SVM model classification principle.

Kernel functions can be broadly divided into three categories: polynomial kernel functions, Gaussian kernel functions, and sigmoid kernel functions. The following Table 1 shows the applicability of kernel function selection in the case of nonlinear separability:

Table 1. Description of the applicability of nuclear functions.

Number	Name of Kernel Function	Advantages	Disadvantages
1	Linear kernel	Few parameters, fast speed	Only linearly separable problems can be solved
2	Polynomial kernel	Solve nonlinear problems	Many parameters, low speed
3	Gaussian kernel	Maps to infinite-dimensional decision boundaries	Prone to overfitting
4	Sigmoid kernel	Reduce overfitting	Non-local optimal

The probability distribution of the multivariate fusion feature matrix and the vertical distribution of the box are obtained by MATLAB processing as shown in Figures 7 and 8.

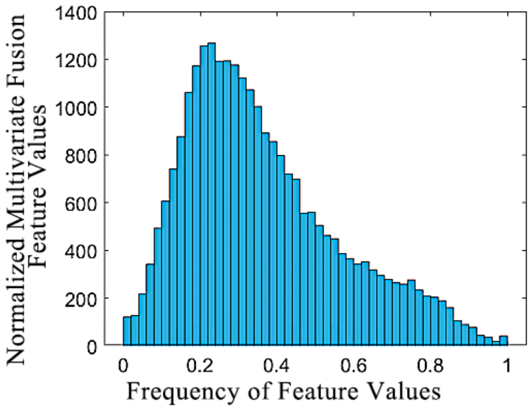

Figure 7. The overall data distribution of multivariate fusion feature matrix.

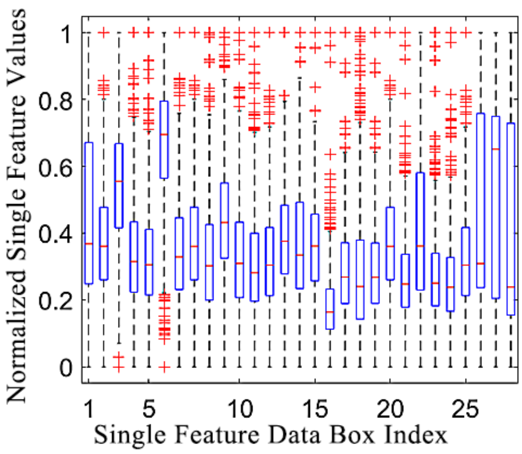

Figure 8. Vertical distribution map of single feature data box.

Analysis of Figure 7 reveals that by attenuating the impact of the number of normalized feature data aggregations, thereby facilitating observation of the global feature data attributes, a probability distribution mirroring a positively skewed Gaussian distribution emerges. This observation underscores the elevated stochasticity inherent in the response signal post-bolt loosening. Furthermore, in conjunction with Figure 8, it is discerned that the interquartile range and extreme values of individual feature groups also encompass the absolute probability interval of the comprehensive dataset, with a negligible incidence of outliers surpassing the established bounds. A holistic assessment, encompassing both the global data distribution and the localized single-group data profiles, corroborates their congruence with the Gaussian distribution paradigm. Consequently, this study selects the Gaussian kernel function for the transformation of the feature matrix into a high-dimensional kernel space.

Given the insufficiency of the conventional SVM approach to discern bolt failure states, the one-vs-one (OVO) classification strategy is implemented. The OVO-SVM methodology necessitates the construction of $n(n-1)/2$ binary SVM classifiers, each dedicated to discriminating between every pair of loose-state feature classes, with classification outcomes adjudicated via a "voting" paradigm. A pre-established classification accumulator is utilized to preserve the "voting results". Subsequently, test set samples are concurrently inputted into the suite of $n(n-1)/2$ trained binary SVM classifiers. Each SVM classifier transmits its decision to the classification accumulator, which increments its count over $n(n-1)/2$ iterations, culminating in a comparison of the accumulated scores. The classification output emanating from the accumulator, exhibiting the maximum accumulated value, signifies the state recognition outcome. The OVO-SVM technique, employing a "voting-based" scheme for pattern differentiation, significantly mitigates classification errors and concomitantly enhances classification accuracy.

2.3. Bolt Vibration Response Test

Taking the bolt joint of the vibrating screen as the object of study, measurement points were arranged for the acquisition and analysis of the vibration response signals of the bolt structure. The sensors were placed on the combine according to the specific location shown in Figure 9, and the 1A312E three-way acceleration sensor, DH5902 acquisition instrument, and DHDAS dynamic acquisition system are connected by custom wire to start the combine harvester working smoothly.

Figure 9. Distribution of vibrating screen bolt measurement points.

The analytical orientation of the experiments was defined as follows: the direction of the combine harvester's travel served as the *X*-axis; the direction perpendicular to the lateral side of the harvester was designated as the *Y*-axis; and the upward vertical direction, perpendicular to the ground, was established as the *Z*-axis. To ensure the integrity and validity of the experimental signal acquisition, triaxial piezoelectric accelerometers (Model 1A312E), developed by Jiangsu Donghua Vibration Testing Co. (Jingjiang, China), were employed. The primary objective of the experiment was to investigate the vibrational response signals of bolted structures at various locations along different axes. Consequently, the sensors were configured to simultaneously measure and output acceleration signals in the X, Y, and Z directions, mutually orthogonal to one another, thereby providing a comprehensive dataset for subsequent effective analysis of the vibrational response. The key specifications of the triaxial accelerometer are detailed in Table 2.

Table 2. The main specifications and parameters of acceleration sensor.

Order	Technical Indicator	Unit	Main Specifications
1	Model		1A312E
2	Range	m/s^2	5000
3	Frequency	Hz	0.5~10,000
4	Dimensions	mm	16.5 × 16.5 × 16.5
5	Weight	g	15
6	Operating temperature	°C	−40~+120
7	Resolution	m/s^2	0.01

After the bolt structure failure response signal is stable, the recording and acquisition will be started. The sampling frequency of the system is set to 2 kHz and continuous sampling for five minutes. After each round of response signal acquisition, the system stops working. The torque wrench is used to adjust the pre-tightening state of the bolt, and the state is set according to the three states of complete preloading, loosening and complete loosening respectively.

The scope of this study is primarily focused on the 4LZY-1.8(PRO688Q) combine harvester. However, the findings and methodology presented herein may serve as a basis for the fault diagnosis of bolt loosening in other machinery. The specifications of the machine and relevant component parameters are listed in Table 3:

Table 3. The specifications of combine harvester 4LZY-1.8(PRO688Q).

Main Working Parts	Main Indicators	Unit	Main Specifications
Engine	Engine model		2403-M-DI-TE2-CKMS3
	Output power	KW (PS)	50 (68)
	Maximum speed	r/min	2700
Threshing device	Threshing method		Axial Flow Type (Rod and Tooth)
	Rotor speed	r/min	560
	Screening method		Vibrating Screen, Airflow (3-Level Airflow Separation)

3. Results and Discussion

3.1. Critical Failure State Analysis

The critical loosening torque of the bolt is as follows:

$$T_s = \frac{1}{3} F_Q \tan(\lambda + \rho) \frac{\left(d^3 - {d_1}^3\right)}{\left(d^2 - {d_1}^2\right)} + \frac{1}{3} \mu_2 F_Q \tan(\lambda + \rho) \frac{\left({d_m}^3 - {d_n}^3\right)}{\left({d_m}^2 - {d_n}^2\right)} \tag{24}$$

K is the torque coefficient, dimensionless, responding to the relationship between the critical torque and the bolt, calculated as follows:

$$K = \frac{T}{F_Q \cdot d} = \frac{\frac{P}{\pi d_2} + \frac{\mu_1}{\cos\beta}}{3d\left(1 - \frac{P}{\pi d_2} \frac{\mu_1}{\cos\beta}\right)} \cdot \left[\frac{\left(d^3 - {d_1}^3\right)}{\left(d^2 - {d_1}^2\right)} + \mu_2 \frac{\left({d_m}^3 - {d_n}^3\right)}{\left({d_m}^2 - {d_n}^2\right)}\right] \tag{25}$$

Assuming that the coefficient of friction between the threaded pairs, the coefficient of friction between the bolts and the connected parts, and the preload are the same, the critical torque of bolts with different diameters is calculated, as shown in Figure 10.

Under conditions of constant friction coefficient and preload, an inverse relationship exists between bolt diameter and critical torque. Consequently, the selection of larger diameter bolts necessitates an increase in preload application. Based on the defined critical failure state, analysis of the bolt vibration signal enables the identification of the bolt's failure condition.

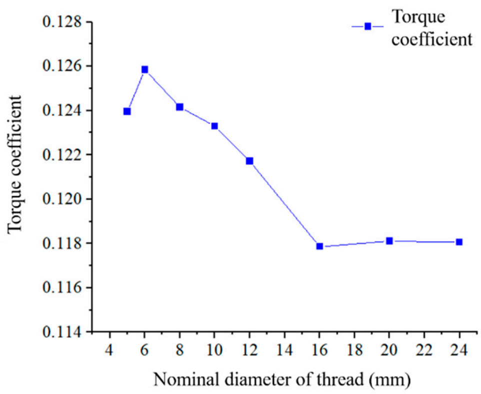

Figure 10. Torque coefficient vs. nominal bolt diameter.

3.2. Vibration Signal Analysis of Vibrating Screen Bolt

3.2.1. Time Domain Characteristics

The time domain signals of the vibrating screen bolt in the three directions of XYZ are shown in Figure 11. The motion form of the vibrating screen can be simplified as an eccentric crank slider mechanism. The whole working part shows a sharp return characteristic during operation, which makes the bolt connection part have a strong load impact and is prone to thread pair damage.

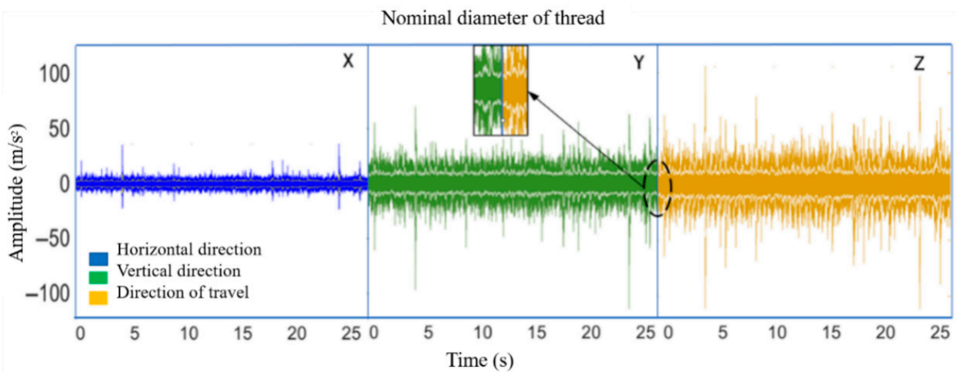

Figure 11. Time domain signals of vibrating screen bolts in X, Y, and Z directions.

As can be seen from Figure 11, the X-direction acceleration response vibration energy is mainly concentrated in 2.84 m/s^2, the Y-direction signal energy intensity is mainly concentrated in 9.73 m/s^2, the Z-direction vibration energy intensity is mainly concentrated in 12.42 m/s^2, and the vibrating sieve bolted joints main vibration direction is for the Z-direction. The impact peak signal not only has strong periodicity but also shows strong asymmetry. The severe impact and collision load in the working process are the main load forms that cause the damage of the thread pair.

3.2.2. Frequency Domain Characteristics

The Z-axis analysis proceeds by examining the vibration energy profile and signal frequency composition. Interference signal constituents are subsequently excised to derive the low-frequency spectral representation depicted in Figure 12. The dominant frequency observed along the Z-axis is 2.32 Hz, corresponding to the reciprocating motion frequency of the vibrating screen. A secondary amplitude peak appears at 37.0794 Hz, equivalent to sixteen times the fundamental reciprocating frequency. Further spectral components may represent the intrinsic natural frequencies of the vibrating screen assembly, as well as component-specific resonant frequencies.

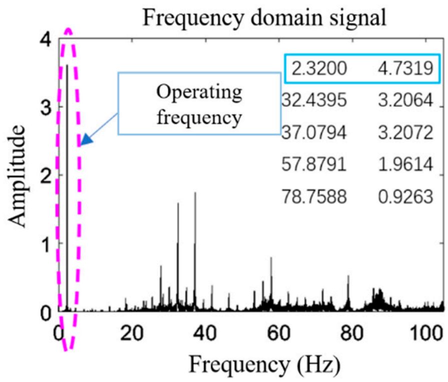

Figure 12. Spectrogram of low-frequency components.

To further elucidate the spatiotemporal distribution of vibration energy within the Z-axis, a short-time Fourier transform (STFT) is applied to the data. The resultant time-frequency characteristics of the vibration energy are then graphically represented as a function of both temporal and spectral domains, as illustrated in Figure 13.

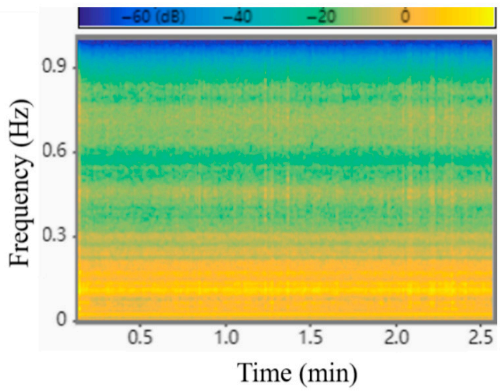

Figure 13. Time-frequency plot.

Time-frequency analysis reveals that the Z-direction response signal exhibits a broad frequency bandwidth, with the strongest signal intensity concentrated in the lower frequency spectrum. A clear staircase pattern, however, is not observed. Comparing the energy distribution across corresponding frequency bands at each measurement location demonstrates the most significant energy gradient in the Z-direction. This suggests that the Z-directional vibration energy is relatively concentrated.

3.3. Bolt Failure State Identification Result Analysis

3.3.1. Time-Frequency Characteristics

To enable a comprehensive analysis, the acquired datasets, representing three discrete operational states—specifically, the tightened, moderately loosened, and fully loosened configurations—were segregated into data1, data2, and data3, respectively. Subsequent to the acquisition of vibration signal data from the vibrating screen's bolted assembly under typical operational circumstances, a time-frequency response assessment was performed, focusing on the Z-axis, which constitutes the primary vibration vector, across the three levels of bolt looseness, as depicted in Figure 14. Spectral scrutiny reveals a progressive enrichment in the frequency content as the looseness escalates, accompanied by a corresponding increase in amplitude. In contrast to the temporal domain representation, the frequency domain depiction provides superior discrimination of the looseness gradation.

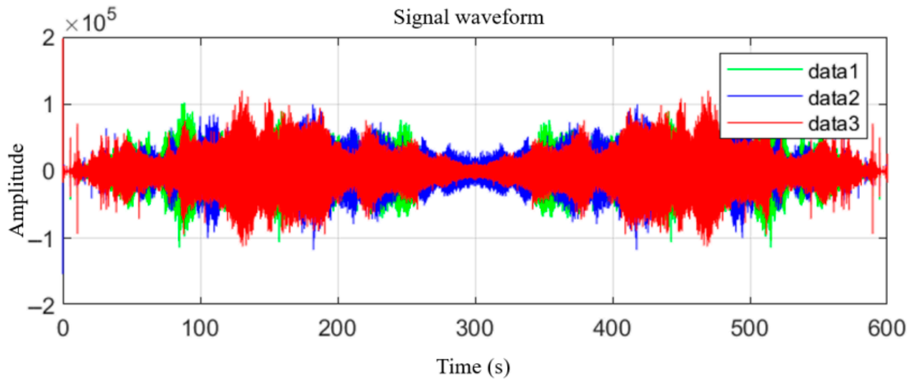

Figure 14. Time-domain signals for different loosening states of the bolt.

Under fully preloaded conditions, the bolted joint presents no normal clearance between its contact surfaces and exhibits minimal tangential displacement, effectively constrained by the small displacement assumption. Consequently, the vibration signature displays minimal amplitude and distinct impulsive characteristics, indicative of a tightly secured assembly. Upon bolt loosening, the pre-tension force diminishes, triggering a cascade of effects: unbalanced collisions, accelerated abrasion, and amplified impact forces across the joint's contact surfaces. This degraded mechanical integrity manifests as a stochastic signal whose amplitude overwhelms that of the vibrating screen's intended operational signal. This obscures the functional signal within the "noise" of the loosening process, resulting in a marked irregularity in the overall vibration signature. While time-domain analysis provides a fundamental distinction between the entirely tightened and generally loosened states, its capacity to discriminate between varying degrees of looseness proves limited. A significant negative bias in the response signal emerges only when the bolt connection has reached a fully loosened configuration. Application of a fast Fourier transform (FFT) to the acquired vibration signal reveals the spectral composition, as detailed in Figure 15. When fully preloaded, the bolted joint exhibits a dominant spectral profile characterized by low-frequency operational and engine rotational frequencies. However, as loosening initiates and progresses, the amplitude and distribution of these frequency components undergo substantial alterations. Specifically, the frequency-domain representation demonstrates that both spectral complexity and overall signal amplitude increase proportionally to the extent of bolt looseness. In direct comparison with time-domain analysis, the frequency-domain approach provides superior granularity and resolution in characterizing and quantifying the degree of bolt loosening.

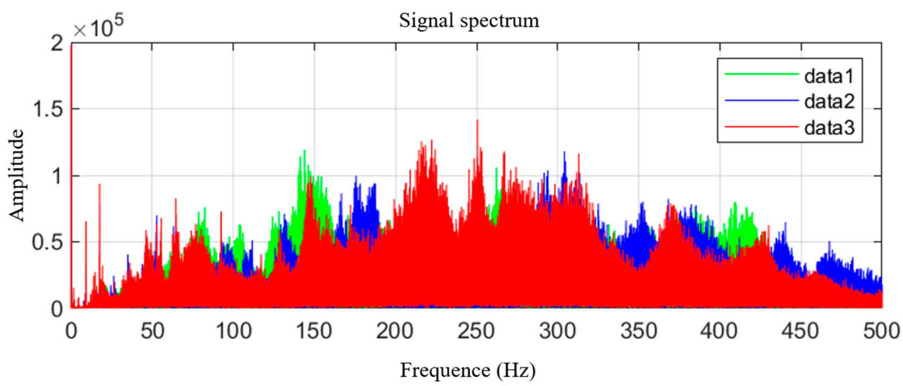

Figure 15. Spectrogram of different loosening states of the bolt.

3.3.2. Secondary Feature Extraction and Matrix Construction

Utilizing MATLAB R2021b software, the VMD algorithm was iteratively applied to the vibration signals acquired under complete loosening, loosening, and fully preloaded conditions, thereby yielding the iterative center frequency values characterizing the three datasets representing the bolted assembly's response. The corresponding spectral curves, illustrating the IMF component decomposition, are presented in Figure 16. The abscissa represents frequency, delineating the distribution of distinct frequency constituents within the IMF components, while the ordinate represents amplitude, signifying the intensity or energy associated with each spectral component. Examination of the FFT-derived outcomes, obtained across varying k values, enables a comprehensive understanding of the signal's frequency-dependent distribution.

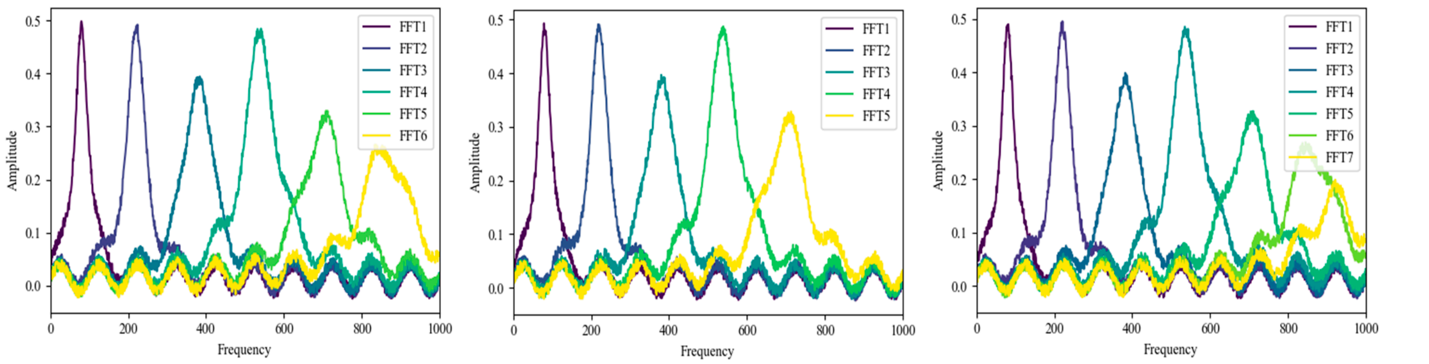

(**a**) k = 6 (**b**) k = 5 (**c**) k = 7

Figure 16. IMF components at different k values. It was observed that the intrinsic mode function (IMF) component frequency bands exhibited significant overlap, and multiple spectral peaks were evident in the spectrum of each IMF component, indicating incomplete signal decomposition. Addressing these limitations, the whale optimization algorithm (WOA) envelope entropy theory was employed to determine the optimal parameter combination for the variational mode decomposition (VMD) algorithm, thus facilitating robust signal feature extraction.

Initially, the number of whale individuals and their multi-dimensional positional representations were initialized. Within the context of this VMD decomposition, the number of whale population members, the dimensionality of the optimization parameters, along with the specified upper and lower bounds of these parameters, were also initialized. Random initialization was applied to the optimal individual position vector and the infinite optimal parameter convergence criterion. Subsequently, iterative optimization was initiated within a loop, enabling the computation of the current fitness function value. In this paper, the envelope entropy (E_p) is selected as the fitness function of the optimization. The envelope entropy represents the sparse characteristics of the signal. When the IMF component has less noise and less feature information, the value of E_p is smaller. In order to minimize the frequency information contained in the obtained IMF component, the envelope entropy minimum ($E_{p_{min}}$) is used as the fitness value. The mathematical principle of E_p is the sequence $\{x_i\}$ obtained by Hilbert demodulation of the initial IMF component is normalized to obtain $\{p_i\}$, and the E_p of the IMF component is calculated. The $E_{p_{min}}$ is found by comparison to complete the calculation of the optimal fitness value.

$$\mathrm{HE} = -\sum_{\mathrm{j}=1}^{\mathrm{K}} \mathrm{P_j}\log(\mathrm{P_j}) \tag{26}$$

Through the VMD decomposition based on WOA optimization, the optimized parameters and the IMF component center frequency values are shown in Table 4.

Table 4. VMD parameters optimized by WOA under different loosening states.

Loose State	Minimum Envelope Entropy	Optimal Penalty Factor	IMF Component Center Frequency/2 kHz							
			K = 1	K = 2	K = 3	K = 4	K = 5	K = 6	K = 7	K = 8
Completely loose	16.6095	1079.1	0.0535	0.0841	0.1565	0.2221	0.2856	0.3669	0.4225	-
Loosening occurs	16.6422	1430.2	0.0763	0.1244	0.1538	0.2642	0.3307	0.405	-	-
Tighten completely	16.6425	1500.0	0.0551	0.098	0.14	0.1839	0.2875	0.3153	0.3764	0.4398

By performing the above optimized VMD decomposition program [48], three sets of IMF component spectrum curves are obtained as shown in Figure 17.

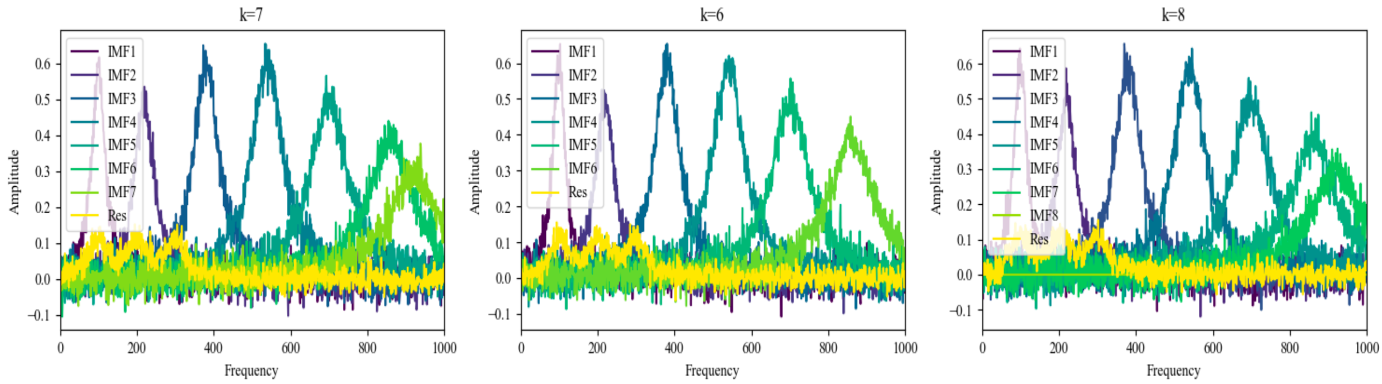

(**a**) k = 7 (**b**) k = 6 (**c**) k = 8

Figure 17. IMF components at different k values. It can be seen from Figure 17 that the IMF component obtained by WOA optimized VMD decomposition can extract the high-frequency components and place the low-frequency components as residuals. This method can filter out the secondary components of the vibration signal, reduce the influence of the interference signal on the vibration signal of the vibrating screen, and clarify the main frequency of the vibration response signal of the vibrating screen bolt loosening state.

3.3.3. Decision Model of Bolt Failure State

To address the inherent irregularities in the raw data and the heterogeneity in the dimensionality of the multi-dimensional dataset, the disparate data aggregations are integrated and reconfigured, culminating in the generation of a high-dimensional matrix encompassing multivariate fusion features, suitable for model training [49,50]. Firstly, time-frequency feature datasets, derived from time-frequency characteristics, are employed to construct high-dimensional feature matrices, designated as A and B, respectively. Subsequently, the energy entropy values associated with IMF1~IMF6 under the fully preloaded state are extracted, yielding feature set C_1. Similarly, energy entropy values derived from IMF1 through IMF6 under the loosened state constitute feature set C_2, while energy entropy values associated with IMF2 through IMF7 under the fully loosened state engender feature set C_3. Subsequently, C_1, C_2, and C_3 are augmented and merged into a quadratic feature extraction matrix, denoted as C. Finally, matrices A, B, and C undergo concatenation and normalization C, thereby culminating in the establishment of a multivariate fusion feature matrix, denoted as G, which is subsequently employed to validate the precision of the recognition model. The underlying operational tenets and procedural steps are delineated as follows:

$$A = \begin{bmatrix} a_{11} & \cdots & a_{1n} \\ \vdots & \ddots & \vdots \\ a_{m1} & \cdots & a_{mn} \end{bmatrix}_{m \times n} \tag{27}$$

$$B = \begin{bmatrix} b_{11} & \cdots & b_{1k} \\ \vdots & \ddots & \vdots \\ b_{m1} & \cdots & b_{mk} \end{bmatrix}_{m \times k} \tag{28}$$

$$C = vertcat(repmat(C_1, m, 1), repmat(C_2, m, 1), repmat(C_3, m, 1)) \tag{29}$$

$$Q_{m \times (n+k+j)} = horzcat(A, B, C) \tag{30}$$

$$L = (L_1 \cdots L_N) = (norm(Q(:, 1)), \cdots, norm(Q(:, n))) \tag{31}$$

$$S = \frac{Q}{repmat(M, m, 1)} \tag{32}$$

$$G = mapminmax(Q) \tag{33}$$

where m is the number of classification groups of the high-vitae enlistment; n is the number of high-vitae enlistment features; [A] is the time-domain feature dataset; [B] is the frequency-domain feature dataset; [C] is the VMD energy-entropy feature dataset; [L] is the high-dimensional feature dataset column vector of the L_2 paradigm vectors; [S] is the L_2 paradigm-normalized high-dimensional feature data matrix; [Q] is the high-dimensional feature dataset; [G] is the normalized high-dimensional feature data matrix; $Vertcat(X_1, \cdots, X_n)$ is to join n same-dimensional matrices vertically; $Horzcat(X_1, \cdots, X_n)$ is to join n same-dimensional matrices horizontally; $Repmat(X,\ n,\ dim)$ is to copy the matrix X n times in rows (dim = 1) or in columns (dim = 2) to form a matrix; $Norm(X)$ is to obtain the paradigm number of the vector X; $minimax$ (X) is to normalize the vector X.

The LIBSVM classification decision model with the embedded OVO-SVM method was selected for training and testing the high-dimensional feature matrix of bolt failure state [51]. The model kernel function was selected as a Gaussian kernel function, and the extracted feature matrices A, B, C and normalized multivariate fusion feature matrix G were trained and tested to verify the sensitivity of different features to the bolt failure state. The identification process of bolt failure status throughout the entire process is shown in Figure 18.

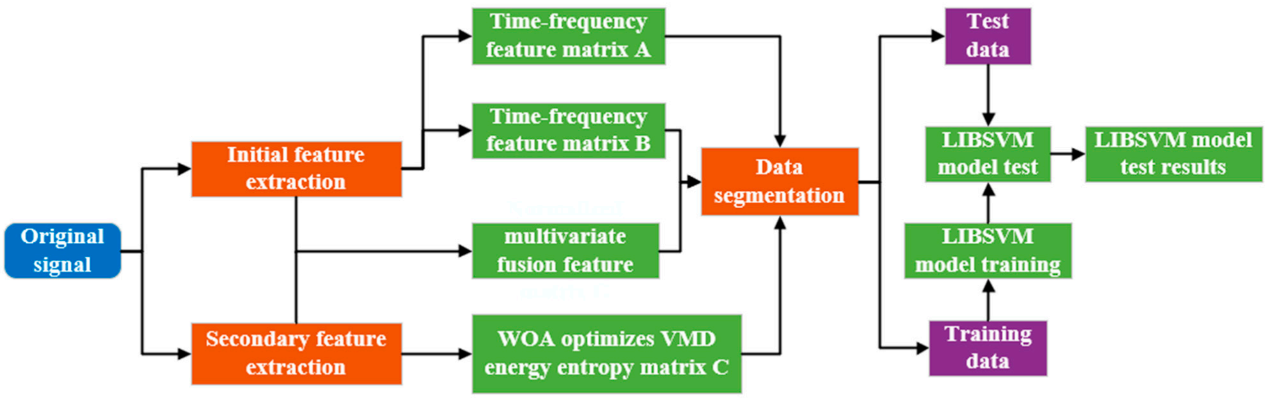

Figure 18. Failure identification method flow of vibrating screen bolts.

Firstly, the high-dimensional feature matrix data undergo labeling: indices 1 through 300 are assigned label 1, indices 301 through 600 are assigned label 2, and indices 601 through 900 are designated as label 3. To maximize the quantity of training samples, thereby satisfying the prerequisites for a globally optimal model, a partitioning strategy is implemented, allocating 90% of the samples to the training subset and extracting the remaining 10% as the test subset. Subsequent to the classification procedure, the recognition success rates and the resultant confusion matrices for the four feature matrix aggregations are obtained, as graphically presented in Figure 19.

Table 5. Confusion matrix for identifying the loose state of the bolt.

Description	Output Class	Target Class 1	Target Class 2	Target Class 3	Precision	Recall/Fallout
	Output Class1	24 (26.7%)	4 (4.4%)	1 (1.1%)	82.8%	80.0%/20.0%
Confusion Matrix 1	Output Class2	6 (6.7%)	23 (25.6%)	18 (20.0%)	48.9%	76.7%/23.3%
	Output Class3	0 (0.0%)	3 (3.3%)	11 (12.2%)	78.6%	36.7%/63.3%
	Output Class1	23 (25.6%)	0 (0.0%)	8 (8.9%)	74.2%	76.7%/23.3%
Confusion Matrix 2	Output Class2	2 (2.2%)	28 (31.1%)	6 (6.7%)	77.8%	93.3%/6.7%
	Output Class3	5 (5.6%)	2 (2.2%)	16 (17.8%)	69.6%	53.3%/46.7%
	Output Class1	23 (25.6%)	10 (11.1%)	0 (0.0%)	69.7%	76.7%/23.3%
Confusion Matrix 3	Output Class2	7 (7.8%)	20 (22.2%)	0 (0.0%)	74.1%	66.7%/33.3%
	Output Class3	0 (0.0%)	0 (0.0%)	30 (33.3%)	100%	100%/0.0%
	Output Class1	30 (33.3%)	0 (0.0%)	0 (0.0%)	100%	100%/0.0%
Confusion Matrix 4	Output Class2	0 (0.0%)	24 (26.7%)	3 (3.3%)	88.9%	80.0%/20.0%
	Output Class3	0 (0.0%)	6 (6.7%)	27 (30.0%)	81.8%	90.0%/10.0%
	Output Class1	59 (32.8%)	0 (0.0%)	0 (0.0%)	100%	98.3%/1.7%
Confusion Matrix 5	Output Class2	0 (0.0%)	59 (32.8%)	0 (0.0%)	100%	98.3%/1.7%
	Output Class3	1 (0.6%)	1 (0.6%)	60 (33.3%)	96.8%	100%/0.0%
	Output Class1	59 (32.8%)	0 (0.0%)	0 (0.0%)	100%	98.3%/1.7%
Confusion Matrix 6	Output Class2	0 (0.0%)	59 (32.8%)	0 (0.0%)	100%	98.3%/1.7%
	Output Class3	1 (0.6%)	1 (0.6%)	60 (33.3%)	96.8%	100%/0.0%

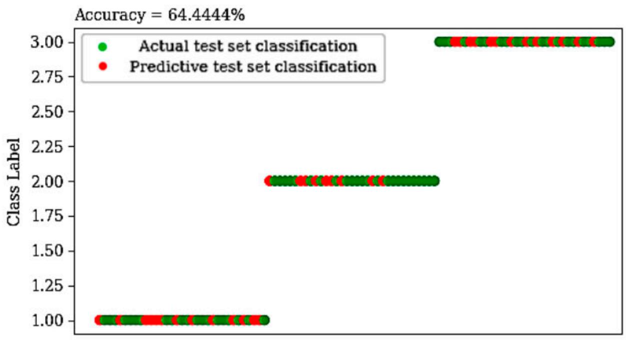

(**a**) Time-domain identity matrix A

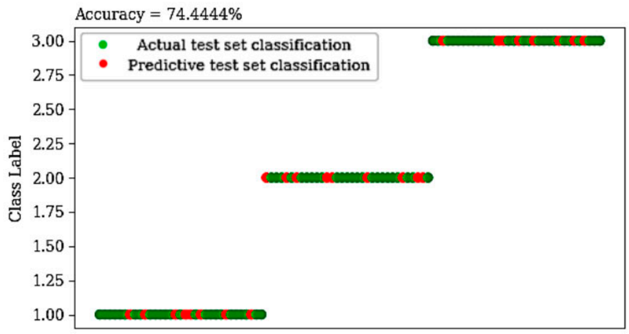

(**b**) Frequency domain identity matrix B

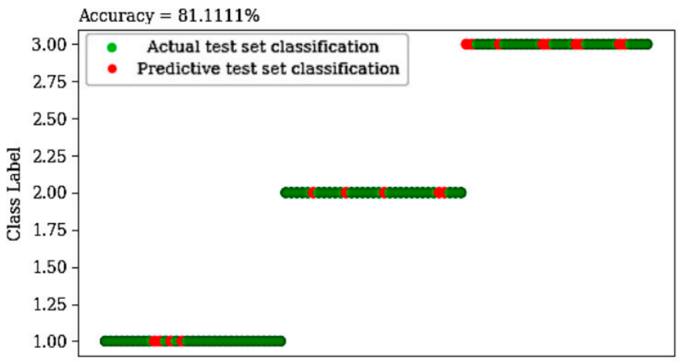

(**c**) VMD energy entropy characterization matrix C

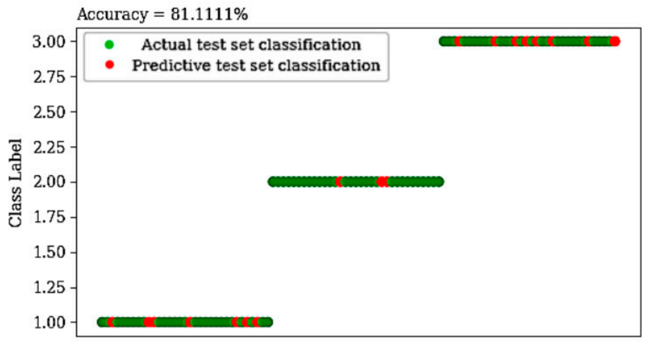

(**d**) Multiple fusion characterization matrix G

Figure 19. Recognition success rate of LIBSVM model for four feature datasets. As demonstrated in figure, matrix A exhibits a suboptimal performance with a minimum training and testing accuracy of only 64.444%. While matrix B similarly reflects modest results, the notable improvement observed with matrix A lends credence to the assertion that frequency domain features possess a superior discriminatory capacity compared to time domain characteristics. Furthermore, the inadequacy of relying solely on a single feature for accurate bolt loosening state identification is substantiated. The WOA-VMD energy entropy matrix C achieves an 81.111% state recognition success rate, yet the enhanced 90% success rate obtained through the normalized multivariate fusion feature matrix G underscores the practical applicability of a multivariate approach for bolt loosening state recognition. The detailed results are documented in Table 5.

4. Conclusions

In this paper, a bolt failure state identification and fault diagnosis method is proposed for the phenomenon that the vibrating screen bolt is prone to failure under multiple excitations, as follows:

(1) The mechanical model of the bolt connection of the combined vibrating screen is established. The relationship between the bolt tightening loose torque and the nominal diameter of the bolt is derived through mathematical analysis so as to determine the initial torque state of the bolt in the vibration signal acquisition experiment. By carrying out the vibration signal acquisition test of the vibrating screen bolt under normal working conditions, it is determined that the main vibration direction of the vibrating screen bolt is the Z-direction, and the working frequency is 2.32 Hz. The Z-direction shows significant impact and asymmetry, which is the most important load form that causes the damage of the thread pair.

(2) The characteristic signal acquisition of the three loose states of the main vibration direction of the vibrating screen bolt is carried out, and the VMD decomposition algorithm based on WOA envelope entropy is used to analyze the optimal parameter combination of the frequency domain curve, filter out the interference signal, extract the characteristics of the vibration signal, and clarify the main frequency of the vibration response signal of the bolt loosening state.

(3) The Gaussian function is selected as the kernel function, and the LIBSVM classification decision model embedded with the OVO-SVM method is proposed to identify and classify the bolt loosening state, and the high-dimensional feature matrix is constructed for model training. The normalized multivariate fusion feature matrix is used to identify the bolt loosening state, and the success rate can reach 90%.

Author Contributions: Conceptualization, J.X.; methodology, Z.T. and J.X.; validation, T.J., J.X. and M.F.; formal analysis, P.L. and J.X.; data curation, T.J., J.X. and P.L.; investigation, T.J. and P.L.; writing—original draft preparation, J.X. and P.L.; writing—review and editing, J.X.; supervision, J.X. All authors have read and agreed to the published version of the manuscript.

Funding: This research work was supported by the Higher Vocational Technical College (Shanghai University of Engineering Science), and the Key Laboratory Equipment of Modern Agricultural Equipment and Technology (Jiangsu University), Ministry of Education (MAET202326).

Institutional Review Board Statement: Not applicable.

Data Availability Statement: The data used to support the findings of this study are available from the corresponding author upon request.

Conflicts of Interest: The authors declared that there are no conflicts of interest.

References

1. Ma, Z.; Wu, Z.; Li, Y.; Song, Z.; Yu, J.; Li, Y.; Xu, L. Study of the grain particle-conveying performance of a bionic non-smooth-structure screw conveyor. *Biosyst. Eng.* **2024**, *238*, 94–104. [CrossRef]
2. Li, Y.; Xu, L.; Lv, L.; Shi, Y.; Yu, X. Study on Modeling Method of a Multi-Parameter Control System for Threshing and Cleaning Devices in the Grain Combine Harvester. *Agriculture* **2022**, *12*, 1483. [CrossRef]
3. Lin, H.; Duan, Y.; Man, Z.; Zareef, M.; Wang, Z.; Chen, Q. Quantitation of volatile aldehydes using chemoselective response dyes combined with multivariable data analysis. *Food Chem.* **2021**, *353*, 129485. [CrossRef] [PubMed]
4. Li, Y.; Liu, Y.; Ji, K.; Zhu, R. A Fault Diagnosis Method for a Differential Inverse Gearbox of a Crawler Combine Harvester Based on Order Analysis. *Agriculture* **2022**, *12*, 1300. [CrossRef]
5. Li, H.; Chen, L.; Zhang, Z. A Study on the Utilization Rate and Influencing Factors of Small Agricultural Machinery: Evidence from 10 Hilly and Mountainous Provinces in China. *Agriculture* **2023**, *13*, 51. [CrossRef]
6. Tang, Z.; Zhang, H.; Zhou, Y.; Li, Y. Mutual Interference and Coupling Response of Multicylinder Vibration among Combine Harvester Co-Frame. *Shock Vib.* **2019**, *2019*, 1584391. [CrossRef]

7. Chandio, F.A.; Li, Y.; Xu, L.; Ma, Z.; Ahmad, F.; Cuong, D.M.; Lakhiar, I.A. Predicting 3D forces of disc tool and soil disturbance area using fuzzy logic model under sensor based soil-bin. *Int. J. Agric. Biol. Eng.* **2020**, *13*, 77–84. [CrossRef]
8. Wang, J.; Hu, B.; Huang, Q.; Zhu, R.; Fu, Q. Simulation analysis and experimental verification on bearings fatigue life of a centrifugal pump. *J. Drain. Irrig. Mach. Eng.* **2024**, *42*, 865–871.
9. Shen, X.; Lu, L.; Zeng, D. Fatigue failure analysis of high strength bolts used for high-speed railway vehicle braking discs. *Eng. Fail. Anal.* **2020**, *115*, 104661. [CrossRef]
10. Fang, P.; Cai, Y.; Chen, L.; Wang, H.; Li, Y.; Sotelo, M.A.; Li, Z. A high-performance neural network vehicle dynamics model for trajectory tracking control. *Proc. Inst. Mech. Eng. Part D J. Automob. Eng.* **2023**, *237*, 1695–1709. [CrossRef]
11. Liu, Y.; Wang, Y.; Ma, G.; Wang, B.; Du, X.; Shi, Q.; Ni, J.; Mao, H. Mechanical properties of stem and physiological–biochemical responses of cucumber under different N and K conditions. *Qual. Assur. Saf. Crop. Foods* **2022**, *14*, 64–74. [CrossRef]
12. Ma, Z.; Zhang, Z.; Zhang, Z.; Song, Z.; Liu, Y.; Li, Y.; Xu, L. Durable Testing and Analysis of a Cleaning Sieve Based on Vibration and Strain Signals. *Agriculture* **2023**, *13*, 2232. [CrossRef]
13. Yang, C.; Chen, H.; Ou, J. Experimental study on seismic performance of modular steel construction beam-to-beam combined side column joint with blind bolted connection. *Thin-Walled Struct.* **2023**, *184*, 110431. [CrossRef]
14. Teng, S.; Wang, Y.; Wei, X.; Du, D. Optimization of forming process for bracket welded parts based on star point design and response surface method. *J. Plast. Eng.* **2024**, *31*, 50–59.
15. Wang, Y.; Li, H.; Jiang, W.; Wang, R.; Li, Y. Dynamic characteristics of an underframe inerter-based suspended equipment for high speed trains. *J. Vib. Shock.* **2022**, *41*, 246–254.
16. Wang, S.; Zhang, Q.; Shi, D.; Yin, C.; Li, C. Analysis of nonlinear vibration response characteristics of hybrid transmission system with dual-planetary gear sets. *J. Jilin Univ. Eng. Technol. Ed.* **2024**, *54*, 890–901.
17. Zhang, A.; Liu, J.; Chen, Z.; Chen, T. Bending behavior of detachable tapered-head bolt inter-module connection of steel modular structure. *J. Constr. Steel Res.* **2024**, *220*, 108829. [CrossRef]
18. Yang, C.; Wang, X.; Wang, Q.; Ou, J. Seismic performance of cruciform bolted joints with various reinforcing details in modular steel construction. *Eng. Struct.* **2023**, *285*, 116069. [CrossRef]
19. Ma, Q.; Wang, K.; Liu, H.; Cheng, Z. Influence of shaft combined misalignment on vibration and noise characteristics in a marine centrifugal pump. *J. Low Freq. Noise Vib. Act. Control* **2022**, *41*, 1286–1306. [CrossRef]
20. Ren, N.; Qiu, Z.; Wang, Y.; He, K. Analysis of Acoustic Field Characteristics of Irregular Multi-inclinedWall Cavity Based on Analytical Method. *Noise Vib. Control* **2020**, *40*, 54.
21. Feng, Q.; Yang, Z.; Guo, W.; Lu, J.; Liang, Y.; Lei, X. Analysis of vertical vibration band gap characteristics of periodic discrete support rail. *Sci. Sin. Technol.* **2020**, *50*, 1563–1576. [CrossRef]
22. Liu, Z.; Huang, X.; Zhao, L.; Wen, G.; Feng, G.; Zhang, Y. Research on online monitoring technology for transmission tower bolt looseness. *Measurement* **2023**, *223*, 113703. [CrossRef]
23. Zhang, B.; Huang, H.; Cai, J.; Jiang, Z.; Zhu, F.; Tang, S.; Qian, P. Multi-dimensional isolation performances of a redundant 6DOF parallel vibration isolation platform. *J. Vib. Shock.* **2022**, *41*, 26–32.
24. Barabadi, M.; Radad, M.; Kahoo, A.R. Seismic data AVO analysis in time frequency domain using synchroextracting transform. *J. Appl. Geophys.* **2024**, *224*, 105364. [CrossRef]
25. Ma, Y.; Yu, G.; Lin, T.; Sun, M. A high-resolution time-frequency analysis technique based on bi-directional squeezing and its application in fault diagnosis of rotating machinery. *ISA Trans.* **2024**, *147*, 382–402. [CrossRef]
26. Pei, J.; Zhang, M.; Wu, C.; Yuan, S.; Dai, Q.; Zhong, Z.; Wang, W. Design and development of vibration monitoring system for Huai'an No.1 Station pump unit based on LabVIEW. *J. Drain. Irrig. Mach. Eng.* **2023**, *41*, 217–223.
27. Zhang, B.; Dai, T.; Tan, C.; Li, J.; Zhang, Y.; Li, S. Non-stationary Pseudo Excitation Method for Analyzing Vibration Characteristics of Suspension System. *J. Vib. Meas. Diagn.* **2022**, *42*, 227–234.
28. Xia, Y.-K.; Wang, W.-T.; Li, X.-Y. Adaptive Parameter Selection Variational Mode Decomposition Based on Bayesian Optimization and Its Application to the Detection of ITSC in PMSM. *IEEE Access* **2024**, *12*, 38594–38614. [CrossRef]
29. Xue, H.; Ding, D.; Li, R.; Xu, X. Feature Extraction Method Based on Component Weighted Reconstruction and Sparse NMF for Bearing Compound Faults of In-wheel Motor. *J. Mech. Eng.* **2023**, *59*, 146–156.
30. Yu, Z.; Li, Y.; Du, X.; Liu, Y. Threshing cylinder unbalance detection using a signal extraction method based on parameter-adaptive variational mode decomposition. *Biosyst. Eng.* **2024**, *244*, 26–41. [CrossRef]
31. Sarothi, S.Z.; Ahmed, K.S.; Khan, N.I.; Ahmed, A.; Nehdi, M.L. Machine learning-based failure mode identification of double shear bolted connections in structural steel. *Eng. Fail. Anal.* **2022**, *139*, 106471. [CrossRef]
32. Chen, D.; Yuan, S.; Pei, J.; Wang, W. Identification method for centrifugal pump working condition based on im-proved binary tree support vector machine. *J. Drain. Irrig. Mach. Eng.* **2023**, *41*, 8–15.
33. Liu, P.; Wang, X.; Wang, Y.; Zhu, J.; Ji, X. Research on percussion-based bolt looseness monitoring under noise interference and insufficient samples. *Mech. Syst. Signal Process.* **2023**, *208*, 111013. [CrossRef]

34. Kaisar, T.I.; Zaman, K.; Khasawneh, M.T. A new approach to probabilistic classification based on gaussian process and support vector machine. *Comput. Ind. Eng.* **2024**, *186*, 109719. [CrossRef]
35. Wang, Z.; Liu, C.; Zhao, W.; Song, X. Rolling bearing fault diagnosis with multi-scale multi-task attention convolu-tional neural network. *Electr. Mach. Control* **2024**, *28*, 65–76.
36. Wan, H.-P.; Gan, J.-R.; Zhu, Y.-K.; Meng, Z. SS-MASVM: An advanced technique for assessing failure probability of high-dimensional complex systems using the multi-class adaptive support vector machine. *Comput. Methods Appl. Mech. Eng.* **2024**, *418*, 116568. [CrossRef]
37. Qian, P.; Pu, C.; Liu, L.; Lu, P.; He, D.; Zhang, B. Sliding Mode Motion Trajectory Tracking Control of a Novel High-Frequency Longitudinal Vibration Friction-Reducing Pneumatic Cylinder. *J. Xi'an Jiaotong Univ.* **2022**, *56*, 22–30.
38. Hu, X.; Zhao, M.; Du, X.; Hu, J.; Zhong, L.; Zhang, W.; Shi, M. Damping and optimization of grain flow sensor gantry based on acoustic black hole. *J. Anhui Agric. Univ.* **2024**, *51*, 523–529.
39. Lou, C.; Lou, C.; Xie, X.; Xie, X. Multi-view universum support vector machines with insensitive pinball loss. *Expert Syst. Appl.* **2024**, *248*, 123480. [CrossRef]
40. Qi, G.; Zhao, Z.; Zhang, R.; Wang, J.; Li, M.; Shi, X.; Wang, H. Optimized VMD algorithm for signal noise reduction based on TDLAS. *J. Quant. Spectrosc. Radiat. Transf.* **2024**, *312*, 108807. [CrossRef]
41. Chen, Y.X.; Chen, L.; Wang, R.C.; Xu, X.; Shen, Y.J.; Liu, Y.L. Modeling and test on height adjustment system of electrically-controlled air suspension for agricultural vehicles. *Int. J. Agric. Biol. Eng.* **2016**, *9*, 40–47. [CrossRef]
42. Acquah, S.J.; Yan, H.; Zhang, C.; Wang, G.; Zhao, B.; Wu, H.; Zhang, H. Application and evaluation of Stanghellini model in the determination of crop evapotranspiration in a naturally ventilated greenhouse. *Int. J. Agric. Biol. Eng.* **2018**, *11*, 95–103. [CrossRef]
43. Majumdar, P.; Mitra, S.; Mirjalili, S.; Bhattacharya, D. Chapter 6 Whale optimization algorithm comprehensive meta analysis on hybridization, latest improvements, variants and applications for complex optimization problems. In *Handbook of Whale Optimization Algorithm*; Mirjalili, S., Ed.; Academic Press: Cambridge, MA, USA, 2024; pp. 81–90.
44. Bonah, E.; Huang, X.; Yi, R.; Aheto, J.H.; Osae, R.; Golly, M. Electronic nose classification and differentiation of bacterial foodborne pathogens based on support vector machine optimized with particle swarm optimization algorithm. *J. Food Process. Eng.* **2019**, *42*, 13236. [CrossRef]
45. Tunio, M.H.; Gao, J.; Lakhiar, I.A.; Solangi, K.A.; Qureshi, W.A.; Shaikh, S.A.; Chen, J. Influence of Atomization Nozzles and Spraying Intervals on Growth, Biomass Yield, and Nutrient Uptake of Butter-Head Lettuce under Aeroponics System. *Agronomy* **2021**, *11*, 97. [CrossRef]
46. Kutsanedzie, F.Y.; Chen, Q.; Hassan, M.; Yang, M.; Sun, H.; Rahman, H. Near infrared system coupled chemometric algorithms for enumeration of total fungi count in cocoa beans neat solution. *Food Chem.* **2018**, *240*, 231–238. [CrossRef]
47. Bai, S.; Yang, Q.; Niu, K.; Zhao, B.; Zhou, L.; Yuan, Y. Discrete Element-Based Optimization Parameters of an Experimental Corn Silage Crushing and Throwing Device. *Trans. ASABE* **2021**, *64*, 1019–1026. [CrossRef]
48. Pan, J.; Le, W.; Wang, Z.; Chen, J. Mathematical model for predicting fungal growth and decomposition rates based on improved Logistic equations. *Int. J. Agric. Biol. Eng.* **2023**, *16*, 60–65. [CrossRef]
49. Yang, N.; Qian, Y.; El-Mesery, H.S.; Zhang, R.; Wang, A.; Tang, J. Rapid detection of rice disease using microscopy image identification based on the synergistic judgment of texture and shape features and decision tree–confusion matrix method. *J. Sci. Food Agric.* **2019**, *99*, 6589–6600. [CrossRef]
50. Cai, Z.; Sun, C.; Zhang, Y.; Shi, R.; Zhang, J.; Zhang, H.; Li, J. Fast detection of the early decay in oranges using visible-LED structured-illumination imaging combined with spiral phase transform and feature-based classification model. *Int. J. Agric. Biol. Eng.* **2024**, *17*, 185–192. [CrossRef]
51. Liang, J.; Zhang, Q.P.; Gu, X.Y. Classification of Asphalt Pavement Defects for Sustainable Road Development Using a Novel Hybrid Technology Based on Clustering Deep Features. *Sustainability* **2024**, *16*, 10145. [CrossRef]